






High-pressure induced Weyl semimetal phase in 2D Tellurium

Chang Niu ^{1,2}, Zhuocheng Zhang^{1,2}, David Graf ³, Seungjun Lee ⁴, Mingyi Wang⁵, Wenzhuo Wu⁵, Tony Low ^{4,6} & Peide D. Ye ^{1,2}✉

Relativistic Weyl fermion quasiparticles in Weyl semimetal bring the electron's chirality degree of freedom into the electrical transport and give rise to exotic phenomena. A topological phase transition from a topological trivial phase to a topological non-trivial phase offers a route to control electronic devices through its topological properties. Here, we report the Weyl semimetal phase in hydrothermally grown two-dimensional Tellurium (2D Te) induced by high hydrostatic pressure (up to 2.47 GPa). The unique chiral crystal structure gives rise to chiral fermions with different topological chiral charges ($C = -1, +1, \text{and } -2$). The highly tunable chemical potential in 2D Te provides comprehensive information for understanding the pressure-dependent electron band structure. The pressure-induced insulator-to-metal transition, two-carrier transport, and the non-trivial π Berry phase shift in quantum oscillations are observed in the 2D Te Weyl semimetal phase. Our work demonstrates the pressure-induced bandgap closing in the inversion asymmetric narrow bandgap semiconductor 2D Te.

¹Elmore Family School of Electrical and Computer Engineering, Purdue University, West Lafayette, IN 47907, USA. ²Birck Nanotechnology Center, Purdue University, West Lafayette, IN 47907, USA. ³National High Magnetic Field Laboratory, Tallahassee, FL 32310, USA. ⁴Department of Electrical and Computer Engineering, University of Minnesota, Minneapolis, MN 55455, USA. ⁵School of Industrial Engineering, Purdue University, West Lafayette, IN 47907, USA. ⁶Department of Physics, University of Minnesota, Minneapolis, MN 55455, USA. ✉email: yep@purdue.edu

The discovery of non-trivial topological electronic structures in quantum materials, such as topological insulators¹, Dirac^{2,3}, Weyl^{4,5}, and nodal-line semimetals, has triggered worldwide interest due to their intriguing physical properties and potential applications. Many quantum materials with topological non-trivial phases, including graphene^{6,7}, Bi₂Te₃⁸, Cd₃As₂^{9,10}, and TaAs^{4,5}, have been extensively investigated. Furthermore, the topological non-trivial phase can also be realized from the topological trivial phase through a topological phase transition by changing the electric field¹¹, chemical composition^{12,13}, or pressure^{14–16}. Besides angle-resolved photoemission spectroscopy (ARPES), understanding of this topological phase transition process by direct electrical transport measurement is essential for studying fundamental physics and developing new topological electronic devices.

In this paper, we investigate the magneto-transport of the Weyl semimetal phase transition of the hydrothermally grown two-dimensional (2D) Tellurium (Te) under high hydrostatic pressure (up to 2.47 GPa) with electrical transport measurement and theoretical calculation. The highly tunable chemical potential of the 2D Te controlled by the back-gate voltage provides an effective way to obtain a comprehensive picture of the semiconductor to Weyl semimetal phase transition in 2D Te under high pressure. A π Berry phase shift in the Shubnikov-de Haas (SdH) oscillations is observed in the 2D Te Weyl semimetal phase under the pressure of 2.17 and 2.47 GPa. Pressure, temperature, magnetic field, and carrier density dependence of the magneto-resistance and Hall resistance are used to analyze this topological phase transition in 2D Te.

Results and discussion

2D Te and high-pressure measurement. The crystal structure of Te is shown in Fig. 1a. Elemental Te in ambient pressure has a trigonal structure formed by Van der Waals interaction between covalently bonded helical Te atomic chains. Based on the chirality^{17,18}, Te falls into two different space groups, P3₁21 (right-handed screw axis) and P3₂21 (left-handed screw axis). Figure 1b is an optical image of the hydrothermally grown 2D Te (sample S2B2np00) with a thickness of around 12 nm. The white arrows indicate the crystal orientation x - and z -direction¹⁹. Electrons (holes) are confined by geometry and gate electric field, giving rise to the two-dimensional electron (hole) gas in the x - z plane. A standard six-terminal Hall-bar device structure (Fig. 1c) with 90 nm SiO₂ as a back-gate dielectric is used for high-pressure, low-temperature magneto-transport measurements. The current is along the helical atomic chain direction z . Figure 1d shows a cartoon schematic of the high-pressure experiment setup. The 2D Te device surrounded by the hydrostatic fluid (Daphne 7575 oil) is mounted into a piston-cylinder pressure cell with insulated transport wires which enables the electrical measurements (see “Methods” and Fig. S1 for details). The magnetic field is applied perpendicular to the sample, which is the y -direction of the Te crystal in Fig. 1a.

It is theoretically predicted that a Weyl semimetal or a nodal-line semimetal formed by the gap closing in inversion asymmetric semiconductors is universal²⁰. The Weyl semimetal phase of Te under pressure is one of the examples. Figure 1e is the theoretically calculated electron band structures of Te in k_z - k_x plane. The lowest unoccupied states and the highest occupied states are located near the H (H') point of the first Brillouin zone, which is not a time-reversal invariant momenta^{16,21–23}. The two spin-split conduction bands cross at H (H') point²⁴ due to the strong spin-orbit interaction²⁵. At ambient pressure, Te is a semiconductor²⁶ with a bandgap of 0.32 eV. With the pressure increase, the shape of the conduction and valence band becomes

sharp. The bandgap decreases and then closes at 2.17 GPa^{16,27,28}. The system experiences a topological phase transition from a semiconductor to a Weyl semimetal when the bandgap is closed. The highest pressure used in our experiment is 2.47 GPa measured at 1.5 K. This paper does not consider the structural phase transition from the trigonal phase Te (I) to a monoclinic phase Te (II) which happens at the pressure of 4 GPa²⁹. The pressure-dependent study on 2D Te with nanoscale structural deformation differs from that in bulk materials³⁰. We investigated the mesoscopic magneto-transport in such a system, providing an example for engineering 2D electron systems in a new degree of freedom.

Topological phase transition in 2D Te under pressure. The longitudinal resistance (R_{zz}) of sample S2B2np00 as a function of the back-gate voltage V_g at different pressures from 0 GPa to 2.47 GPa is shown in Fig. 2a. We are able to access both the valence band and the conduction band by applying a back-gate voltage V_g in all the pressures at 1.5 K. At ambient pressure, a typical semiconducting transport behavior is expected. With increasing pressure, the bandgap decreases and closes at 2.47 GPa, resulting in a maximum sheet resistance of only 2500 Ω (about 0.1 h/e^2) across the whole gate voltage range. The discontinuity at pressures lower than 2.47 GPa is caused by the insulating state when the chemical potential is tuned inside the bandgap. To further investigate the bandgap closing in 2D Te under pressure, we performed the two-terminal differential conductance (dI/dV) measurement³¹ between the source and the drain electrodes (Fig. 1c) at 1.5 K. A dc voltage bias V_b and a small ac excitation dV were applied at the drain. The ac current dI through the channel was measured with the back-gate voltage V_g controlling the chemical potential of the 2D Te. Figure 2b shows the band diagram of the differential conductance measurement at 0 GPa and 2.47 GPa, respectively. The system has a low conductivity if no states are available in 2D Te. When the band edge (valence or conduction) enters the source-drain energy window (eV_b), ac current dI increases sharply. We set the bias voltage V_b at 0 mV and the small ac excitation dV at 1 μ V. The differential conductance dI/dV in log scale as a function of the back-gate voltage V_g is shown in Fig. 2c. Because of the bandgap, at 0 GPa and V_g around 6 V, the system is nearly insulating with the differential conductance below 0.01 μ S, limited by the electrical measurement setup. On the other hand, the minimum conductance at 2.47 GPa is over three orders of magnitude larger, indicating a phase change from semiconductor to semimetal in 2D Te.

The pressure-induced insulator-to-metal transition is also observed in the temperature dependence of the longitudinal resistance R_{zz} at $V_g = 0$ V. Figure 2d shows the normalized longitudinal resistance ($R_{zz}(T)/R_{zz}(150\text{ K})$) under different pressures. The R_{zz} increases upon cooling at the pressure of 0 GPa and 0.4 GPa (measured in two different thermal cycles), which is typical for a semiconductor. A transition to positive dR_{zz}/dT emerges with the increasing pressure. In addition, the positive dR_{zz}/dT is seen in both electron dominant ($V_g = 40$ V) and hole dominant ($V_g = -20$ V) 2D Te, as shown in Fig. 2e. Similar metallic temperature-dependent transport is measured in another 2D Te device (S1B3nn00) under the pressure of 2.17 GPa (Fig. S2). The semimetal phase is reached at the pressure of 2.17 GPa in 2D Te, which quantitatively agrees with our DFT calculations (~ 2.0 GPa).

In the Weyl semimetal phase of Te, the monopole-antimonopole pair of Weyl nodes are located at four P points related by the C_2 rotation and time-reversal symmetry¹⁶ as illustrated in Fig. 3a. The band crossing at H (H') point with two-dimensional irreducible representation H_6 is also a Weyl point due to the chiral crystal structure of Te. When the band inversion

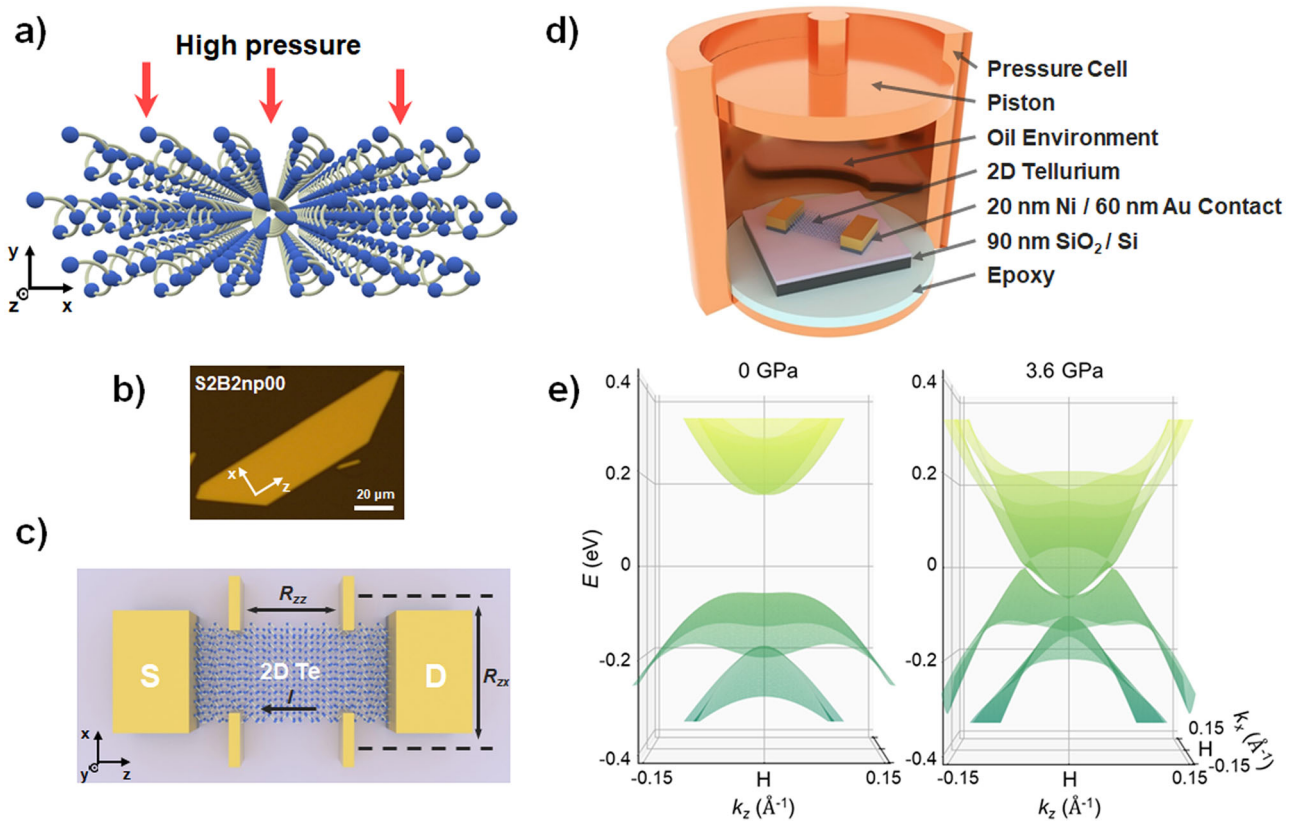


Fig. 1 Experiment schematic and 2D Te under pressure. **a** Crystal structure of right-handed Te with spiral atomic chains. **b** An optical image of sample S2B2np00 with crystal orientation indicated by the white arrows. **c** The structure of a six-terminal Hall-bar 2D Te device. R_{zz} and R_{zx} represent the longitudinal and transverse resistance. I is the probing current. **d** Schematic configuration of the piston-cylinder pressure cell. The sample is fixed on the pressure cell platform with insulated transport wires which enable the electrical transport measurement. A PTFE cup filled with oil is placed over the sample platform so the device is surrounded by the hydrostatic fluid. A hydraulic press is used to add pressure with a piston. **e** Theoretically calculated electron band structures of Te around H (H') point in k_x - k_y plane at ambient pressure (0 GPa) and high-pressure (3.6 GPa), showing the pressure-induced bandgap closing and band deformation.

happens under high pressure, the band crossing at H point becomes threefold, giving rise to unconventional chiral fermions with high topological chiral charges ($|C| = 2$)^{16,32}. As the gap closing in Te involves two spin-split conduction bands and one valence band, the bands are gapped between H point and P point, resulting in three Fermi surfaces (one electron-like and two hole-like) around the H (H') point, as shown in the calculated Fermi surface (Fig. 3b). When the chemical potential controlled by the back-gate voltage V_g lies between two gapped bands, transport involving both electrons and holes is expected. An anomaly in the gate-dependent Hall resistance (R_{zx}) of 2D Te under the pressure of 2.47 GPa is observed at 1.5 K (Fig. 3c). The nonlinear Hall resistance is antisymmetric with respect to the magnetic field B (Fig. S3), which exclude the nonlinear effect from the device structure asymmetry or the pressure non-uniformity. Instead of continuous growth in the Hall coefficient $|R_H|$ as the back-gate voltage sweeps from -40 V to positive bias, the decrease at 10 V is caused by the increase of electron density. A crossover from the hole dominant transport to electron dominant transport is observed at $V_g = 20$ V. A two-carrier transport model³³ is used to analyze the nonlinear Hall resistance. The magneto-transport in a two-carrier semimetal is given by:

$$R_{zx} = \frac{(p\mu_n^2 - n\mu_e^2)B + (p - n)\mu_n^2\mu_e^2B^3}{e[(n\mu_e + p\mu_n)^2 + (p - n)^2\mu_n^2\mu_e^2B^2]} \quad (1)$$

where e is the elementary charge, B is the magnetic field, n (p) is the electron (hole) density, and μ_e (μ_h) is the electron (hole)

mobility. Figure 3d shows the nonlinear fitting of the Hall resistance at the hole dominant regime ($V_g = -30$ V) by Eq. (1). At $V_g = 40$ V, the chemical potential shifts away from the Weyl nodes in P point where the hole pockets are depleted (Fig. 3b), and an electron density of $6.0 \times 10^{12} \text{ cm}^{-2}$ is calculated from $\frac{1}{eR_H}$, where R_H is the linear fitting slope of the Hall resistance. The electron and hole density (mobility) extracted from the Hall measurement as a function of the back-gate voltage is plotted in Fig. 3e (Fig. S4). By changing the chemical potential, the Fermi surface evolution of both electrons and holes fits well with the theoretical calculations, providing strong evidence for observing the Weyl semimetal phase in 2D Te. Fig. S2c shows another sample (S1B3nn00) with similar nonlinear Hall resistance under the pressure of 2.17 GPa.

Quantum oscillations and non-trivial π Berry's phase in 2D Te

Weyl semimetal phase. The relatively high carrier mobility in 2D Te leads to the observation of SdH oscillation, which reveals the cyclotron properties and the electron band information. Figures 4a, b show the back-gate voltage dependence of the SdH oscillation amplitude ΔR_{zz} after subtracting the magneto-resistance in two different 2D Te devices: S1B3nn00 at 2.17 GPa and S2B2np00 at 2.47 GPa (see Fig. S5 for the complete mapping). Coherent oscillations with discrete Landau levels from $n = 6$ are observed. A degeneration of 4 containing two-fold valley degeneracy and two hole-like pockets can be concluded by comparing the oscillation density with the carrier density. The

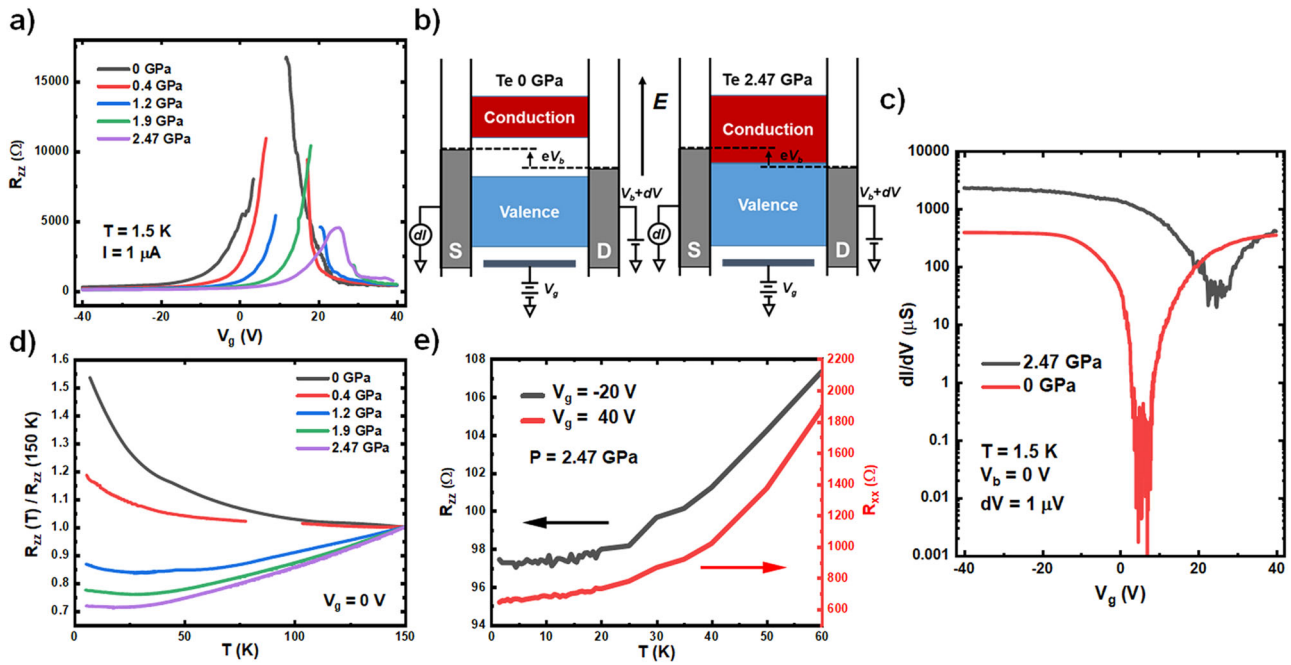


Fig. 2 Bandgap closing and insulator to metal transition in 2D Te under pressure. **a** The longitudinal resistance (R_{zz}) as a function of back-gate voltage V_g at different pressures from 0 GPa to 2.47 GPa. The temperature is 1.5 K. **b** Schematic band diagram of 2D Te field-effect transistor in a differential conductance (dI/dV) measurement setup at 0 GPa and 2.47 GPa. The current dI is determined by the dc bias voltage V_b , the small ac excitation dV , and the gate voltage V_g . **c** Back-gate voltage V_g dependence of the differential conductance (dI/dV) at $V_b = 0$ V. The temperature is 1.5 K and the ac excitation dV is 1 μ V. Over 3 orders of magnitude difference in conductance minima at low temperature indicates the bandgap is closed in 2D Te under high pressure (2.47 GPa). **d** Temperature dependence of the normalized longitudinal resistance ($R_{zz}(T)/R_{zz}(150$ K)) at different pressures. The insulator-to-metal transition is observed. **e** Temperature dependence of the longitudinal resistance (R_{zz}) at $V_g = -20$ V and $V_g = 40$ V. Both electrons and holes have metallic behavior at high pressure (2.47 GPa).

oscillations in Fig. 4a, b originate from the hole-like pocket in the Te Weyl semimetal phase because the oscillation frequency B_F (proportional to the oscillation density) decreases with the increasing back-gate voltage V_g . By electrostatic gating, the oscillations from the electron-like pocket are shown in Fig. S6. It is worth mentioning that the electron-like Fermi surface encloses a Weyl node (at H point) with a monopole charge of two when the bandgap closes, making 2D Te an ideal system for investigating the electrical transport of unconventional chiral fermions³². The SdH oscillation amplitude ΔR_{zz} follows the Onsager-Lifshitz quantization rule:

$$\Delta R_{zz} \propto \cos\left(2\pi\left(\frac{B_F}{B} + \frac{1}{2}\right) + \varphi\right) \quad (2)$$

where φ is the oscillation phase. We calculated the Fermi surfaces and Berry curvature distributions near the Weyl points shown in Fig. S7, indicating that the Weyl points act as either a sink or a source of Berry curvature. Electrons in an external magnetic field picked up a Berry's phase during the cyclotron motion along the Fermi surface, resulting in a π -phase shift in quantum oscillations, which is one of the electrical transport signatures of the non-trivial topological band structure widely observed in many Dirac or Weyl quantum materials^{3,6,34,35} as well as in n-type 2D Te²⁴. The Landau fan diagram of two 2D Te devices under different gate voltages with the minima (maxima) in the SdH oscillation assigned to integer (half-integer) are shown in Fig. 4c, d. The Linear fitting of the Landau level n as a function of $1/B$ has an intercept around 0.5 (Fig. 4e, f), corresponding to an oscillation phase $\varphi = \pi$. On the contrary, no oscillation phase shift is observed in the same sample (S2B2np00) under ambient pressure (Fig. S8) or in the previous work on p-type 2D Te³⁶, making the π phase shift in quantum oscillations under 2.47 GPa a strong

evidence for the topologically non-trivial Weyl semimetal phase. Furthermore, the quantum oscillation phase extracted from all pressures at different back-gate voltages (see Fig. S9 for details) is plotted in Fig. 4f. The pressure-induced topological phase transition from semiconductor ($\varphi \sim 0$ with cold colored signs) to Weyl semimetal ($\varphi \sim \pi$ with warm colored signs) is clearly observed.

Using the temperature dependence of the quantum oscillation amplitude ΔR_{zz} the cyclotron effective mass m^* is extracted under different pressures (Fig. S10) by fitting the thermal damping term in the L-K formula:

$$\Delta R_{zz} \propto \frac{2\pi^2 m^* k_B T / \hbar e B}{\sinh(2\pi^2 m^* k_B T / \hbar e B)} \quad (3)$$

as shown in Figs. S11 and S12. The effective mass decreases to 0.20 m_0 (where m_0 is the free electron mass) at 2.47 GPa. We attribute this effective mass change to the band deformation^{16,27} in 2D Te under high pressure. The shape of the conduction and valence band in 2D Te becomes sharp as the bandgap closes. The abrupt drop in effective mass after 1.9 GPa potentially reveals another evidence of the band structure transition from a semiconductor to a Weyl semimetal.

Based on the evidence of gap closing in differential conductance, temperature-dependent insulator to metal transition, two-carrier transport, band deformation, and the non-trivial π Berry phase in quantum oscillations, we unambiguously demonstrate that a topological phase transition from a semiconductor to a Weyl semimetal in 2D Te occurs under high hydrostatic pressure. It shows the potential to controllably change the topological properties of semiconducting materials with inversion asymmetric structure for novel electronic device applications using pressure, strain, or other methods.

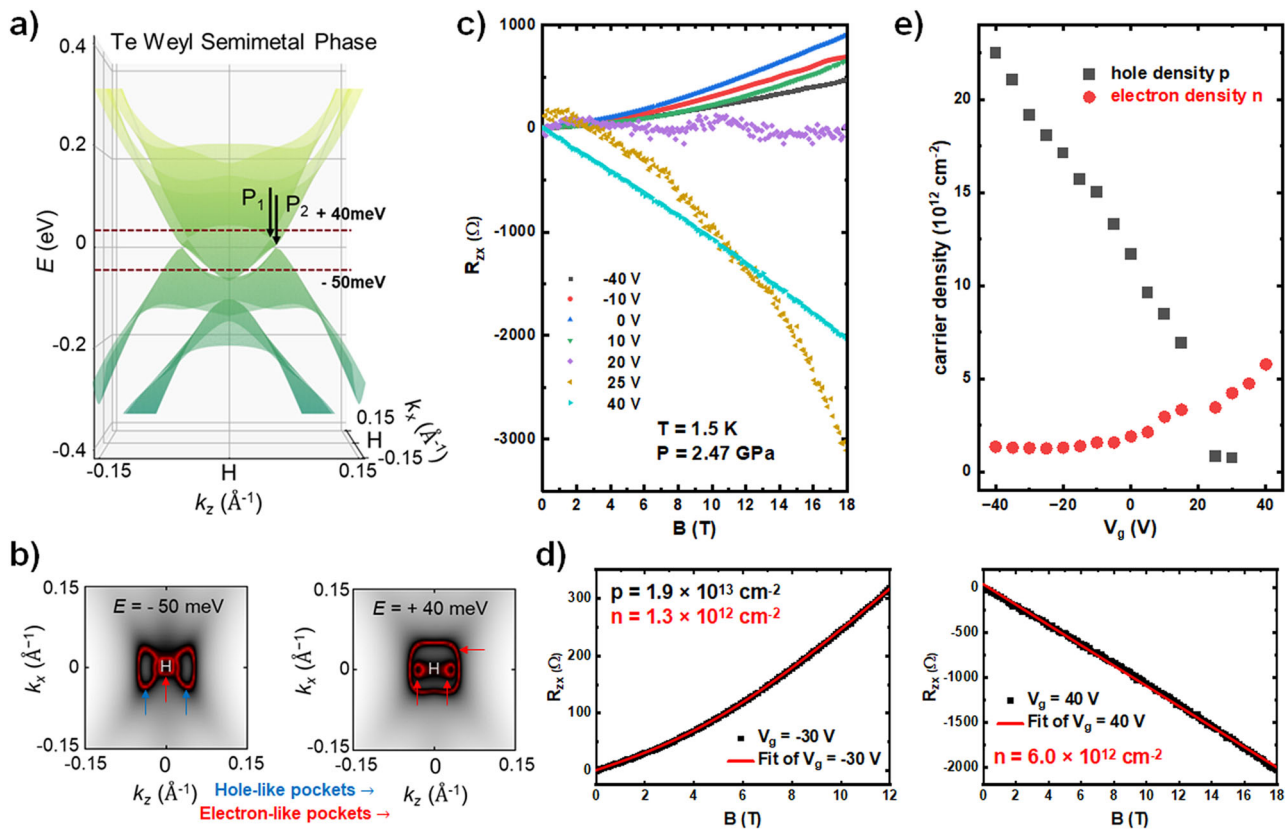


Fig. 3 Nonlinear Hall resistance and two-carrier transport in 2D Te under pressure (2.47 GPa). **a** Electron band diagram of Te Weyl semimetal phase around H (H') point. Two hole-like pockets and one electron-like pocket appear due to the bandgap closing. **b** Fermi surface mappings at different energies ($E = -50$ and 40 meV). The blue and red arrows indicate the hole-like pockets and electron-like pockets, respectively. **c** Transverse resistance (R_{xy}) as a function of magnetic field B at different back-gate voltages from -40 V to 40 V. **d** Two-carrier transport model and linear fitting of the Hall data (red lines) at $V_g = -30$ V and $V_g = 40$ V, respectively. **e** Electron and hole density as a function of gate voltages extracted from the Hall data.

Methods

Hydrothermal growth of 2D Te flakes. 0.5 g of polyvinylpyrrolidone (PVP) (Sigma-Aldrich) and 0.09 g of Na_2TeO_3 (Sigma-Aldrich) were dissolved in 32 ml double-distilled water. 3.33 ml of aqueous ammonia solution (25–28%, w/w%) and 1.67 ml of hydrazine hydrate (80%, w/w%) were added to the solution under magnetic stirring to form a homogeneous solution. The mixture was sealed in a 50 ml Teflon-lined stainless steel autoclave and heated at 180°C for 30 h before naturally cooling down to room temperature.

Device fabrication. Te flakes were transferred onto 90 nm SiO_2/Si substrate. The six-terminal Hall-bar devices were patterned using electron beam lithography and metal contacts were deposited by electron beam evaporation. 20/60 nm Ni/Au was used as an electrical contact for 2D Te.

High-pressure experiment setup. The device is diced or cut to size to fit within the 3.0 mm sample space of the piston-cylinder pressure cell. A fiber optic has a small ruby chip fixed to the tip which is used to calibrate the pressure at room temperature and again at low temperature. The device is fixed to this fiber optic and the insulated transport wires of the pressure cell platform with epoxy to orient the device so the applied magnetic field will be perpendicular to the sample. Thin platinum wires are soldered to the copper wires of the sample platform. The free ends of the platinum wires are then attached to the contact pads with silver paint. A Polytetrafluoroethylene (PTFE) cup is filled with Daphne 7575 oil and fixed in place over the sample platform so the device is surrounded by

the hydrostatic fluid. When the pressure cell is fully assembled a hydraulic press is used to add pressure with a piston through a hole in the threaded top screw of the cell. When the appropriate pressure is reached, the top screw is clamped, locking in the pressure.

Low-temperature magneto-transport measurements. The low-temperature high-pressure magneto-transport measurements were performed in the 18 T superconducting magnet system (SCM2) with the Variable Temperature Insert (VTI) at the National High Magnetic Field Laboratory (NHMFL) in Tallahassee, FL. The electrical data were acquired by standard small signal ac measurement technique using SR830 lock-in amplifiers (Stanford Research). The dI/dV measurement was performed using SR860 lock-in amplifiers (Stanford Research) with 0 mV dc bias and 1 μV ac excitation at 8.777 Hz.

First-principles calculations. To understand the topological phase transition of 2D Te, we performed first-principles calculations based on density functional theory³⁷ as implemented in the Vienna ab initio simulation package (VASP)³⁸. The projector augmented wave potentials^{39,40} were used to describe the valence electrons and the plane-wave kinetic energy cutoff was chosen to be 400 eV. In a structure relaxation, the exchange-correlation function was treated by the generalized gradient approximation of Perdew-Burke-Ernzerhof (PBE)⁴¹. The equilibrium lattice constant of bulk Te was calculated to be $a = 4.507$ Å and $c = 5.960$ Å. To describe 2D Te under strain, we applied a biaxial strain along the hexagonal plane of Te to preserve its hexagonal symmetry. The lattice constant along c was freely relaxed under the biaxial

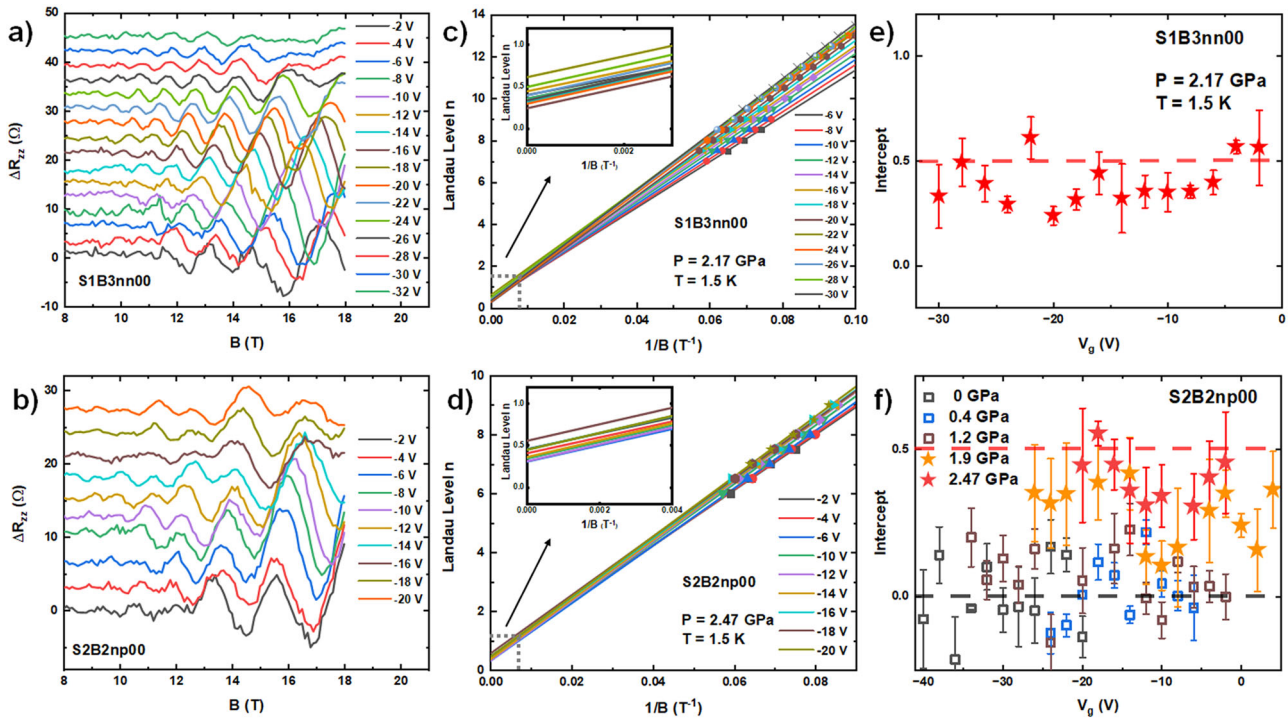


Fig. 4 Quantum oscillations and non-trivial π Berry's phase in pressure-induced 2D Te Weyl semimetal phase. Back-gate voltage V_g dependence of the Shubnikov-de Haas (SdH) oscillation (ΔR_{zz}) with background subtracted in two different samples **a** S1B3nn00 at 2.17 GPa and **b** S2B2np00 at 2.47 GPa. The curves are shifted for clarity. The temperature is 1.5 K. **c, d** Landau fan diagram of two samples under different back-gate voltages. The minima and maxima in the SdH oscillations are assigned with integer and half-integer respectively. Straight lines are linear fitting under each gate voltage. Insets: magnified views of gray dashed boxes. **e, f** Intercept of the linear fittings as a function of back-gate voltage V_g in two different samples. The error bars represent the standard errors in the linear fit. A phase shift from 0 to π in SdH oscillations indicates the pressure-induced topological transition in 2D Te.

strain. The obtained lattice constants and volume of bulk Te are summarized in Fig. S13 in SI. The electronic structures were calculated by meta-GGA density functional (modified Becke-Johnson potential^{42,43}) with spin-orbit interaction, which ensures a better accuracy than PBE and is less expensive than HSE06 (Fig. S14). To investigate the effects of the thickness of strained 2D Te (Fig. S15) and Berry phase physics (Fig. S7), we constructed a first-principles tight binding model using Wannier90 package^{44,45}. For the wannierization, we used s and p orbital projections for all Te atoms. The momentum-dependent Berry curvature maps and 2D slab electronic structures were calculated using Wanniertools package⁴⁶.

Data availability

All data needed to evaluate the conclusions in the paper are present in the paper and/or the Supplementary Materials.

Code availability

All first-principles calculations were performed by VASP, Wannier90, and WannierTools packages. Additional scripts used in the current study are available from the corresponding author under request.

Received: 24 October 2023; Accepted: 10 November 2023;

Published online: 28 November 2023

References

- Hasan, M. Z. & Kane, C. L. Colloquium: topological insulators. *Rev. Mod. Phys.* **82**, 3045–3067 (2010).
- Young, S. M. et al. Dirac semimetal in three dimensions. *Phys. Rev. Lett.* **108**, 140405 (2012).
- Xiong, J. et al. Evidence for the chiral anomaly in the Dirac semimetal Na₃Bi. *Science* **350**, 413–416 (2015).
- Lv, B. Q. et al. Experimental discovery of weyl semimetal TaAs. *Phys. Rev. X* **5**, 031013 (2015).
- Yang, L. X. et al. Weyl semimetal phase in the non-centrosymmetric compound TaAs. *Nat. Phys.* **11**, 728–732 (2015).
- Zhang, Y., Tan, Y. W., Stormer, H. L. & Kim, P. Experimental observation of the quantum Hall effect and Berry's phase in graphene. *Nature* **438**, 201–204 (2005).
- Novoselov, K. S. et al. Two-dimensional gas of massless Dirac fermions in graphene. *Nature* **438**, 197–200 (2005).
- Chen, Y. L. et al. Experimental realization of a three-dimensional topological insulator, Bi₂Te₃. *Science* **325**, 178–181 (2009).
- Liu, Z. K. et al. A stable three-dimensional topological Dirac semimetal Cd₃As₂. *Nat. Mater.* **13**, 677–As681 (2014).
- Zhang, C. et al. Quantum Hall effect based on Weyl orbits in Cd₃As₂. *Nature* **565**, 331–336 (2019).
- Collins, J. L. et al. Electric-field-tuned topological phase transition in ultrathin Na₃Bi. *Nature* **564**, 390–394 (2018).
- Xu, S. Y. et al. Topological phase transition and texture inversion in a tunable topological insulator. *Science* **332**, 560–564 (2011).
- Xu, S. Y. et al. Observation of a topological crystalline insulator phase and topological phase transition in Pb_{1-x}Sn_xTe. *Nat. Commun.* **3**, 1192 (2012).
- Xi, X. et al. Signatures of a pressure-induced topological quantum phase transition in BiTeI. *Phys. Rev. Lett.* **111**, 155701 (2013).
- Liang, T. et al. A pressure-induced topological phase with large Berry curvature in Pb_{1-x}Sn_xTe. *Sci. Adv.* **3**, 1602510 (2017).
- Hirayama, M. et al. Weyl node and spin texture in trigonal tellurium and selenium. *Phys. Rev. Lett.* **114**, 206401 (2015).
- Bradley, A. J. The crystal structures of the rhombohedral forms of selenium and tellurium. *Lond. Edinb. Dublin Philos. Mag. J. Sci.* **48**, 477–496 (1924).
- Niu, C. et al. Tunable nonreciprocal electrical transport in 2D Tellurium with different chirality. *Nano Lett.* **2201**, 08829 (2022).
- Wang, Y. et al. Field-effect transistors made from solution-grown two-dimensional tellurene. *Nat. Electron.* **1**, 228–236 (2018).

20. Murakami, S. et al. Emergence of topological semimetals in gap closing in semiconductors without inversion symmetry. *Sci. Adv.* **3**, 1602680 (2017).
21. Tsirkin, S. S. et al. Gyrotropic effects in trigonal tellurium studied from first principles. *Phys. Rev. B* **97**, 035158 (2018).
22. Agapito, L. A. et al. Novel family of chiral-based topological insulators: Elemental tellurium under strain. *Phys. Rev. Lett.* **110**, 176401 (2013).
23. Doi, T., Nakao, K. & Kamimura, H. The valence band structure of tellurium. I. The k_p perturbation method. *J. Phys. Soc. Japan* **28**, 36–43 (1970).
24. Qiu, G. et al. Quantum Hall effect of Weyl fermions in n-type semiconducting tellurene. *Nat. Nanotechnol.* **15**, 585–591 (2020).
25. Niu, C. et al. Gate-tunable strong spin-orbit interaction in two-dimensional tellurium probed by weak antilocalization. *Phys. Rev. B* **101**, 205414 (2020).
26. Chen, J. et al. Topological phase change transistors based on tellurium Weyl semiconductor. *Sci. Adv.* **8**, eabn3837 (2022).
27. Ideue, T. et al. Pressure-induced topological phase transition in noncentrosymmetric elemental tellurium. *Proc. Natl. Acad. Sci. USA* **116**, 25530–25534 (2019).
28. Rodriguez, D. et al. Two linear regimes in optical conductivity of a type-I Weyl semimetal: the case of elemental tellurium. *Phys. Rev. Lett.* **124**, 136402 (2020).
29. Akahama, Y., Kobayashi, M. & Kawamura, H. Pressure-induced superconductivity and phase transition in selenium and tellurium. *Solid State Commun.* **84**, 803–806 (1992).
30. Yankowitz, M. et al. Dynamic band-structure tuning of graphene moiré superlattices with pressure. *Nature* **557**, 404–408 (2018).
31. Han, M. Y., Özyilmaz, B., Zhang, Y. & Kim, P. Energy band-gap engineering of graphene nanoribbons. *Phys. Rev. Lett.* **98**, 206805 (2007).
32. Bradlyn, B. et al. Beyond Dirac and Weyl fermions: unconventional quasiparticles in conventional crystals. *Science* **353**, aaf5037 (2016).
33. Qiu, G. et al. Observation of optical and electrical in-plane anisotropy in high-mobility few-layer $ZrTe_5$. *Nano Lett.* **16**, 7364–7369 (2016).
34. Murakawa, H. et al. Detection of Berry's phase in a bulk Rashba semiconductor. *Science* **342**, 1490–1493 (2013).
35. Liang, T. et al. Ultrahigh mobility and giant magnetoresistance in the Dirac semimetal Cd_3As_2 . *Nat. Mater.* **14**, 280–284 (2015).
36. Qiu, G. et al. Quantum transport and band structure evolution under high magnetic field in few-layer tellurene. *Nano Lett.* **18**, 5760–5767 (2018).
37. Kohn, W. & Sham, L. J. Self-consistent equations including exchange and correlation effects. *Phys. Rev.* **140**, A1133–A1138 (1965).
38. Kresse, G. & Furthmüller, J. Efficient iterative schemes for ab initio total-energy calculations using a plane-wave basis set. *Phys. Rev. B* **54**, 11169–11186 (1996).
39. Blöchl, P. E. Projector augmented-wave method. *Phys. Rev. B* **50**, 17953–17979 (1994).
40. Kresse, G. & Joubert, D. From ultrasoft pseudopotentials to the projector augmented-wave method. *Phys. Rev. B* **59**, 1758–1775 (1999).
41. Perdew, J. P., Burke, K. & Ernzerhof, M. Generalized gradient approximation made simple. *Phys. Rev. Lett.* **77**, 3865–3868 (1996).
42. Becke, A. D. & Johnson, E. R. A simple effective potential for exchange. *J. Chem. Phys.* **124**, 221101 (2006).
43. Tran, F. & Blaha, P. Accurate band gaps of semiconductors and insulators with a semilocal exchange-correlation potential. *Phys. Rev. Lett.* **102**, 226401 (2009).
44. Mostofi, A. A. et al. An updated version of wannier90: A tool for obtaining maximally-localised wannier functions. *Comput. Phys. Commun.* **185**, 2309–2310 (2014).
45. Pizzi, G. et al. Wannier90 as a community code: new features and applications. *J. Condens. Matter Phys.* **32**, 165902 (2020).
46. Wu, Q., Zhang, S., Song, H.-F., Troyer, M. & Soluyanov, A. A. Wanniertools: an open-source software package for novel topological materials. *Comput. Phys. Commun.* **224**, 405–416 (2018).

Acknowledgements

P.D.Y. was supported by the Army Research Office under grant no. W911NF-15-1-0574. W.W. was sponsored by the Army Research Office under Grant Number W911NF-20-1-0118. The synthesis of 2D Te was supported by NSF under grant no. CMMI-2046936. A portion of this work was performed at the National High Magnetic Field Laboratory, which is supported by National Science Foundation Cooperative Agreement No. DMR-1644779 and the State of Florida. C.N. and Z.Z. acknowledge technical support from National High Magnetic Field Laboratory Staff Glover Jones.

Author contributions

P.D.Y. conceived and supervised the project. C.N. and P.D.Y. designed the experiments. M.W. and W.W. synthesized the material. C.N. fabricated the devices. C.N., Z.Z., and D.G. performed the magneto-transport measurements under pressure. S.L. and T.L. performed the first-principles calculations. C.N. and P.D.Y. analyzed the data. P.D.Y. and C.N. wrote the manuscript and all the authors commented on it.

Competing interests

The authors declare no competing interests.

Additional information

Supplementary information The online version contains supplementary material available at <https://doi.org/10.1038/s42005-023-01460-1>.

Correspondence and requests for materials should be addressed to Peide D. Ye.

Peer review information This manuscript has been previously reviewed in another Nature Portfolio journal. The manuscript was considered suitable for publication without further review at Communications Physics.

Reprints and permission information is available at <http://www.nature.com/reprints>

Publisher's note Springer Nature remains neutral with regard to jurisdictional claims in published maps and institutional affiliations.



Open Access This article is licensed under a Creative Commons Attribution 4.0 International License, which permits use, sharing, adaptation, distribution and reproduction in any medium or format, as long as you give appropriate credit to the original author(s) and the source, provide a link to the Creative Commons licence, and indicate if changes were made. The images or other third party material in this article are included in the article's Creative Commons licence, unless indicated otherwise in a credit line to the material. If material is not included in the article's Creative Commons licence and your intended use is not permitted by statutory regulation or exceeds the permitted use, you will need to obtain permission directly from the copyright holder. To view a copy of this licence, visit <http://creativecommons.org/licenses/by/4.0/>.

© The Author(s) 2023